

# The FIP and Inverse FIP Effects in Solar Flares

J. MARTIN LAMING<sup>1</sup>

<sup>1</sup>*Space Science Division, Code 7684, Naval Research Laboratory, Washington DC 20375, USA*

Submitted to ApJ

## ABSTRACT

The Inverse First Ionization Potential (FIP) Effect, the depletion in coronal abundance of elements like Fe, Mg, and Si that are ionized in the solar chromosphere relative to those that are neutral, has been identified in several solar flares. We give a more detailed discussion of the mechanism of fractionation by the ponderomotive force associated with magnetohydrodynamic waves, paying special attention to the conditions in which Inverse FIP fractionation arises in order to better understand its relation to the usual FIP Effect, i.e. the enhancement of coronal abundance of Fe, Mg, Si, etc. The FIP Effect is generated by parallel propagating Alfvén waves, with either photospheric, or more likely coronal, origins. The Inverse FIP Effect arises as upward propagating fast mode waves with an origin in the photosphere or below, refract back downwards in the chromosphere where the Alfvén speed is increasing with altitude. We give a more physically motivated picture of the FIP fractionation, based on the wave refraction around inhomogeneities in the solar atmosphere, and inspired by previous discussions of analogous phenomena in the optical trapping of particles by laser beams. We apply these insights to modeling the fractionation and find good agreement with the observations of [Katsuda et al. \(2020\)](#) and [Dennis et al. \(2015\)](#).

*Keywords:* solar wind – Sun: abundances – Sun: chromosphere – turbulence – waves

## 1. INTRODUCTION

The elemental composition of various regions of the solar corona and wind can vary from that of the underlying photosphere, an inference first made by [Pottasch \(1963\)](#). The usually observed anomaly is an overabundance in the corona by a factor of 3-4 relative to the photosphere of elements with first ionization potential (FIP) below about 10 eV, while elements with higher FIP are relatively unaffected. These low FIP elements, like Mg, Si, Fe, are those that can be photoionized by H I Lyman  $\alpha$ , and are predominantly ionized in the chromosphere, while the high FIP elements (e.g. O, Ne, Ar) remain neutral. A mechanism involving ion-neutral separation in the solar chromosphere is clearly indicated. With the launch of the Extreme Ultraviolet Explorer (EUVE) satellite in 1992, similar abundance anomalies were also discovered in the corona of late-type stars (e.g. [Drake et al. 1997](#); [Laming et al. 1996](#); [Laming & Drake](#)

[1999](#)). The increasing spectroscopic precision afforded by the Chandra and XMM satellites allowed the sample of observed stellar coronae to increase and a variation of abundance anomaly with stellar spectral type become apparent. As summarized most recently by [Wood et al. \(2018\)](#), stars of spectral type earlier and up to that of the Sun have a similar FIP related coronal abundance anomaly. As the spectral type becomes later, the FIP Effect decreases, with coronal abundances becoming essentially photospheric at mid-K. For even later spectral types the abundance anomaly inverts, becoming “Inverse-FIP”, with low FIP elements depleted rather than enhanced in abundance in the corona relative to the photosphere, reaching a similar level of depletion, 1/3 - 1/4, to the previously mentioned enhancement.

A similar advance in instrumentation to observe the Sun led to the discovery of Inverse-FIP Effect in solar flares. Using the Hinode/Extreme ultraviolet Imaging Spectrometer (EIS), [Doschek et al. \(2015\)](#) found small patches of enhanced Ar XIV 194.40, 187.96 Å relative to Ca XIV 193.87 Å emission, indicative of an Ar/Ca abundance ratio of seven times the photospheric value, in well

defined structures near sunspots. [Doschek & Warren \(2016\)](#) also find that S behaves more like a low FIP element in Inverse-FIP Effect, i.e. it is depleted, whereas it is well known to behave as a high FIP element in coronal FIP fractionated plasma (e.g. [Laming et al. 1995](#)). [Doschek & Warren \(2017\)](#) find regions of reduced FIP (but not actually Inverse FIP) over larger areas. This echoes the work of [Feldman et al. \(1990\)](#), who found photospheric abundances in the transition region over a sunspot, and argued that the sunspot environment was not conducive to FIP fractionation.

The Inverse-FIP effect has also recently been identified in spatially unresolved regions of solar flare plasma, seen in observations with *Suzaku* by [Katsuda et al. \(2020\)](#). *Suzaku* ([Mitsuda et al. 2007](#)) is a Japanese satellite for X-ray astronomy, that due to its low Earth orbit observed the Earth’s atmosphere illuminated by the Sun for a few minutes each orbit. [Katsuda et al. \(2020\)](#) were able to identify Earth albedo emission recorded during four X class flares in 2005 and 2006 with the X-ray Imaging Spectrometer (XIS [Koyama et al. 2007](#)), and after correcting for scattering and intrinsic albedo emission, isolated the solar emission and measured element abundances. [Dennis et al. \(2015\)](#) see something similar in observations of solar flares by the Solar Assembly for X-Rays (SAX [Schlemm et al. 2007](#)) on the MERcury Surface Space ENvironment GEOchemistry and Ranging (MESSENGER) satellite. They report a transition between fractionated and unfractionated elements at about a FIP of 7 eV rather than 10 eV (i.e. Ca is fractionated, while other low FIPs are not). We will investigate whether this can come about as a combination of Inverse FIP and FIP Effect, which together deplete low FIP elements like Fe and Si more than Ca.

The FIP fractionation has been identified and modeled in a series of papers ([Laming 2004, 2009, 2012, 2015a, 2017; Laming et al. 2019](#)) as being due to the ponderomotive force associated with Alfvénic waves. This separates ions from neutrals in the chromosphere, and the sign of the fractionation depends on the gradient of  $\delta E^2/B^2$ , the square of the wave electric field divided by the square of the ambient magnetic field. As discussed further below, this result is mathematically clear, but physical picture dictating when this gradient should be positive or negative is more obscure, which limits our ability to connect abundance observations with other solar phenomena. Prior work (e.g. [Laming 2015a](#)) has suggested that parallel propagating waves give FIP, because the degree of reflection required to produce Inverse-FIP proved difficult to achieve in Alfvén wave propagation calculations, integrating the transport equations in a model solar chromosphere. The

total internal reflection of initially upward propagating fast mode waves in the chromosphere with Alfvén speed increasing with height appeared to be a plausible Inverse-FIP scenario, investigated further observationally by [Baker et al. \(2019, 2020\)](#). The initially upward propagating waves are posited to have an origin in sub-surface reconnection as neighboring sunspot umbrae interact. This seems more likely than the mode conversion of acoustic waves deriving from photospheric convection in the high plasma  $\beta$  photosphere to fast mode waves above the  $\beta = 1$  layer, since the wave amplitudes resulting from such a process are likely insufficient to cause the fractionation.

In this paper we revisit the FIP and Inverse-FIP effects with a much more physically motivated picture than in previous work. Much insight is drawn from the realization that the ion-neutral separation caused the ponderomotive force is an analog in magnetohydrodynamics (MHD) of phenomena in optical physics related to the trapping and manipulation of particles in the radiation field of a laser (e.g. [Ashkin 1970; Ashkin et al. 1986](#)) that won Nobel Prizes for Steven Chu in 1997 and Arthur Ashkin in 2018.

## 2. THE IMPORTANCE OF PLASMA $\beta < 1$

Figure 1 shows a schematic diagram of magnetic fields (calculated from [Athay 1981](#)) and wave propagation in the solar chromosphere, indicating the key components. Upcoming p-modes mode convert at the layer where sound and Alfvén speeds are equal ( $\beta = 6/5$  in  $\gamma = 5/3$  gas) and propagate into the  $\beta < 1$  region as fast mode waves, where they undergo a total internal reflection. Alfvén waves of coronal origin enter from the top, and are reflected back upwards, and competition between these two wave fields gives the Inverse FIP or FIP fractionation. Here we give some further justification for why fractionation must occur in this region, and not below this layer, even though magnetosonic and Alfvén waves may still propagate there. The ion-neutral separation caused by the ponderomotive force must compete with mixing caused by turbulence. Wave-wave interactions throughout the solar atmosphere can cause a cascade to successively shorter wavelengths and ultimately to fundamental length scales like the mean free path or the gyroradius that can cause microscopic mixing. In the solar photosphere hydrodynamic turbulence dominates, with cascade rate  $\simeq \delta u/L$  (e.g. [Batchelor 1986; Landau & Lifshitz 1987](#)) where  $\delta u$  is the velocity fluctuation amplitude and  $L$  is the eddy scale length. Taking  $\delta u \simeq 0.1 \text{ km s}^{-1}$  ([Reardon et al. 2008](#)) and  $L = 2000 \text{ km s}^{-1}$  to be the wavelength of a 5 minute sound wave gives a cascade rate of  $5 \times 10^{-5} \text{ s}^{-1}$ .

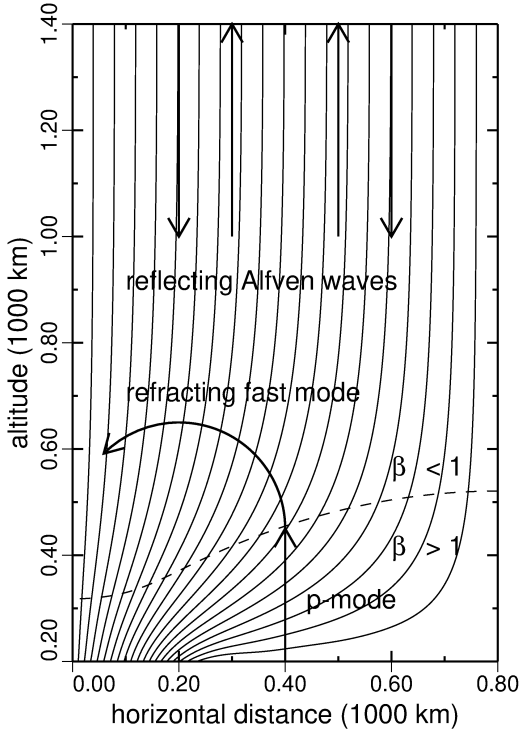


**Figure 1.** Schematic diagram of chromospheric magnetic field lines (solid), equipartition layer (dashed) dividing the  $\beta = 8\pi nk_B T/B^2 \geq 1$  regions, and wave propagations giving rise to competing FIP and Inverse FIP fractionations.

With ponderomotive acceleration  $a$ , the fractionation is given by (e.g. [Laming 2015a](#))

$$f_k = \frac{\rho_k(z_u)}{\rho_k(z_l)} = \exp \left\{ \int_{z_l}^{z_u} \frac{2\xi_k a \nu_{kn} / [\xi_k \nu_{kn} + (1 - \xi_k) \nu_{ki}]}{2k_B T/m_k + v_{||,osc}^2 + 2u_k^2} dz \right\} \quad (1)$$

derived from the momentum equations for ions and neutrals in a background of protons and neutral hydrogen for densities of element  $k$  above ( $\rho(z_u)$ ) and below ( $\rho(z_l)$ ) the fractionation region. In these equations  $\xi_k$  is the ionization fraction of element  $k$ ,  $\nu_{ki}$  and  $\nu_{kn}$  are collision frequencies of ions and neutrals of element  $k$  with the background gas (mainly hydrogen and protons, given by formulae in [Laming 2004](#)),  $k_B T/m_k (= v_z^2)$  represents the square of the element  $k$  thermal velocity along the  $z$ -direction,  $u_k = \partial z / \partial t$  is the upward flow speed and  $v_{||,osc}$  a longitudinal oscillatory speed, corresponding to upward and downward propagating sound waves. The fractionation rate is then given by

$$\frac{\partial \ln f_k}{\partial t} \simeq \frac{2\xi_k a \nu_{kn} / [\xi_k \nu_{kn} + (1 - \xi_k) \nu_{ki}]}{2k_B T/m_k + v_{||,osc}^2 + 2u_k^2} u_k. \quad (2)$$

For closed loops supporting resonant Alfvén waves, the ponderomotive acceleration is strongest in the strong density gradient at the top of the chromosphere with value  $a \simeq 10 \text{ km s}^{-2}$ . Then with  $\xi_k \simeq 1$ ,  $u_k \simeq 0.1 \text{ km s}^{-1}$ , and  $v_{||,osc} \simeq 10 \text{ km s}^{-1}$  the fractionation rate is of order  $0.01 \text{ s}^{-1}$ . Lower down in the chromosphere, closer to the  $\beta = 1$  layer,  $a \simeq 0.1 \text{ km s}^{-2}$  and  $u_k \simeq 0.001 \text{ km s}^{-1}$  giving a rate of order  $10^{-6} \text{ s}^{-1}$ , so clearly such fractionation would not survive against photospheric turbulence.

Alfvén and fast mode waves in the  $\beta < 1$  chromospheric regions may also generate turbulence and mixing, though compared to the hydrodynamic case, the cascade rate is lower (e.g. [Ng & Bhattacharjee 1997](#)) because the interaction time,  $1/k_{||}v_A$ , is usually much less than the eddy turn over time,  $1/k_{\perp}\delta v_{\perp}$ , where the subscripts  $||$  and  $\perp$  refer to the velocity fluctuations and wave vectors parallel to and perpendicular to the magnetic field. If this then requires  $N = (k_{||}v_A/k_{\perp}\delta v_{\perp})^2$  interactions to complete the eddy turn over, the cascade rate in weak turbulence is given by the heuristic expression  $k_{||}v_A/N = (k_{\perp}\delta v_{\perp})^2/k_{||}v_A$ , (e.g. [Beresnyak 2019](#)). A derivation of this expression from quasi-linear plasma wave theory is sketched in the Appendix. The expressions derived in the appendix (Equation A10) and that quoted above coincide for  $k_{\perp}/k_{||} = 1/4\sqrt{2}$ . At the top of the chromosphere where the fractionation rate is maximized,  $\delta v_{\perp} \sim 10 \text{ km s}^{-1}$ ,  $v_A \sim 100 \text{ km s}^{-1}$  and the cascade rate for 5 minute waves is  $1/32 \times 0.02 \times 10^2/100^2 \sim 10^{-5} \text{ s}^{-1}$ , to be compared with a fractionation rate of  $0.01 \text{ s}^{-1}$  estimated above. Closer to the  $\beta = 1$  layer  $\delta v_{\perp} \sim 0.1 \text{ km s}^{-1}$ ,  $v_A \sim 6 \text{ km s}^{-1}$ , and the cascade rate evaluates to  $1/32 \times 0.02 \times 0.1^2/6^2 \sim 10^{-7} - 10^{-6} \text{ s}^{-1}$ , comparable to fractionation rate.

### 3. THE ORIGIN OF THE FIP AND INVERSE FIP EFFECTS: ALL MODELS ARE WRONG, BUT SOME ARE USEFUL!

Wave-wave interactions and turbulence are the most commonly discussed phenomena by which waves modify plasma behavior. The ponderomotive force is seemingly less well known. The ponderomotive force due to optical light was originally invoked by Kepler following the return in 1607 of what we now know to have been Halley's comet to (incorrectly) explain the direction of the comet tail in the solar radiation field ([Ridpath 1985](#))<sup>1</sup>. The ponderomotive force associated with Alfvén waves has mainly seen applications in auroral and magnetospheric physics (see e.g. the review by [Lundin & Guglielmi](#)

<sup>1</sup> John Herschel observing the 1835 return of Halley's comet provided the correct explanation, the solar wind!

2006) who also briefly discuss astrophysical examples such as the collimation of jets, and has been derived in a number of ways. Lundin & Guglielmi (2006) give a derivation considering the single particle motions in the magnetic and electric fields of an Alfvén wave, where the force arises as the  $\delta v_x$  component of the induced particle motion is crossed with the  $\delta B_y$  of the wave motion to give a force along the ambient magnetic field direction,  $\hat{\mathbf{z}}$ . Laming (2009, 2015a) consider the Lagrangian for plasma particles interacting with an Alfvén wave, which requires knowledge of the energy partitioning within the wave. Laming (2017) derives the ponderomotive force from considerations of the polarization and magnetization induced in a medium by waves, and Washimi & Karpman (1976) work from the change in relative permittivity induced by the passage of a wave. These last two only require knowledge of the wave dielectric constant. The derivations are collected in the appendix of Laming (2017), and all agree with equation 30 from the more detailed and general mathematical treatment given by Lee & Parks (1983). The time independent part of their expression is reproduced here,

$$\begin{aligned} f_j &= \frac{1}{16\pi} \left[ (\epsilon_{\beta\alpha} - \delta_{\beta\alpha}) \frac{\partial \delta E_\alpha \delta E_\beta^*}{\partial x_j} \right. \\ &\quad \left. + \frac{\partial}{\partial x_l} \left( \epsilon_{jmp} \epsilon_{klm} B_p \frac{\partial \epsilon_{\beta\alpha}}{\partial B_k} \delta E_\alpha \delta E_\beta^* \right) \right] \\ &= \frac{1}{16\pi} \left[ (\epsilon_{\beta\alpha} - \delta_{\beta\alpha}) \frac{\partial \delta E_\alpha \delta E_\beta^*}{\partial x_j} + \frac{\partial \epsilon_{\alpha\beta}}{\partial \mathbf{B}} \frac{\partial \mathbf{B}}{\partial x_j} \delta E_\alpha \delta E_\beta^* \right] \\ &= \frac{\rho c^2}{2} \frac{\partial}{\partial x_j} \left( \frac{\delta E_\perp \delta E_\perp^*}{B^2} \right), \end{aligned} \quad (3)$$

where  $\epsilon_{xx} = \epsilon_{yy} = \epsilon_{\perp\perp} = 1 + 4\pi\rho c^2/B^2$  is the plasma relative permittivity for  $\delta \mathbf{E}$  perpendicular to the background magnetic field  $\mathbf{B} = B\hat{\mathbf{z}}$ ,  $\delta_{\beta\alpha}$  is the Kronecker delta, and  $\epsilon_{jmp}$  is the Levi-Civita epsilon. Summing is implied over repeated indices.

None of these derivations make any reference to the polarization of the wave, and so we expect the same expression for the ponderomotive force should apply to Alfvén and fast mode waves equally (in conditions where the plasma  $\beta < 1$ ), with any differences in fractionation by these different waves arising from their different propagations through and interactions with other waves in the chromosphere. To emphasize and explore this point, we give here a mathematically less rigorous derivation, but with stronger physical motivation following Ashkin (1970); Ashkin et al. (1986).

Consider first the refraction of fast mode waves around a sphere of higher density and therefore lower Alfvén speed embedded in a medium with magnetic field and gradient of wave energy density in the  $\hat{\mathbf{z}}$  direction, as

in the left panel of Figure 2. We ignore wave reflection at the boundary of the sphere, assume geometrical optics for the wave propagation, and take  $\beta \ll 1$  so that fast modes are essentially isotropic in their propagation. The initial wave direction makes an angle  $\theta_1$  with the normal to the boundary upon entering the sphere at point A, and is refracted to an angle  $\theta_2$ , illustrated by the bold ray. The total deflection of the ray after refracting at entrance and exit is  $2(\theta_1 - \theta_2)$ , for a total longitudinal momentum transfer to the sphere of  $\Delta p_{||} = 2p \sin^2(\theta_1 - \theta_2)$ , where  $p$  is the initial wave momentum (more properly the wave pseudomomentum, Peierls 1991). In conditions of a negative wave energy gradient going upward, a wave with smaller momentum enters at point B, undergoes the same refractions, and would move the sphere downward by a smaller amount, leaving a net upward force.

Writing the spatially varying component of the wave momentum as  $p = -r \cos \theta_1 \times \partial U / \partial z / v_A$  where  $U$  is the wave energy density and  $v_A$  is the Alfvén speed, the rate of momentum change is

$$\begin{aligned} \Delta \dot{p}_{||} &= - \int_0^\pi d\phi \int_{-\pi}^\pi 2 \frac{\partial U}{\partial z} r \cos^2 \theta_1 \times \\ &\quad (\sin \theta_1 \cos \theta_2 - \sin \theta_2 \cos \theta_1)^2 r^2 d\theta_1 \end{aligned} \quad (4)$$

which is multiplied out using  $n_2 \sin \theta_2 / n_1 \sin \theta_1 = 1$  (Snell's Law) to

$$\begin{aligned} \Delta \dot{p}_{||} &= -2\pi r^3 \frac{\partial U}{\partial z} \int_{-\pi}^\pi \sin^2 \theta_1 - \sin^4 \theta_1 + \frac{n_1^2}{n_2^2} (\sin^2 \theta_1 \\ &\quad - 3 \sin^4 \theta_1 + 2 \sin^6 \theta_1) - 2 \frac{n_1}{n_2} \sin^2 \theta_1 \cos^3 \theta_1 \cos \theta_2 d\theta_1. \end{aligned} \quad (5)$$

In the last term we put  $\cos \theta_2 \approx \cos \theta_1$  and integrate to find

$$\Delta \dot{p}_{||} = -4\pi^2 r^3 \frac{\partial U}{\partial z} \left( \frac{1}{8} - \frac{1}{8} \frac{n_1}{n_2} \right). \quad (6)$$

The calculation for Alfvén waves proceeds similarly, except that Snell's Law is now

$$\frac{n_2 \sin \theta_2}{n_1 \sin \theta_1} = \cos \theta_1 \cos \theta_2 + \frac{n_2^2}{n_1^2} \sin \theta_1 \sin \theta_2, \quad (7)$$

derived from equation 11 in Laming (2015b). This applies for initial waves propagating along the magnetic field. Compared to Laming (2015b), the magnetic field does not change direction between the two media, so the notation  $\{\theta_{2w}, \theta_2\}$  in Laming (2015b) goes over to  $\{\theta_2, \theta_1\}$  here. The second refraction on exit is much more complicated, because the initial wave is no longer propagating along the magnetic field. We simply approximate this second refraction as one half of the entrance refraction, which then recovers equation 6 upon integration over angles as before.

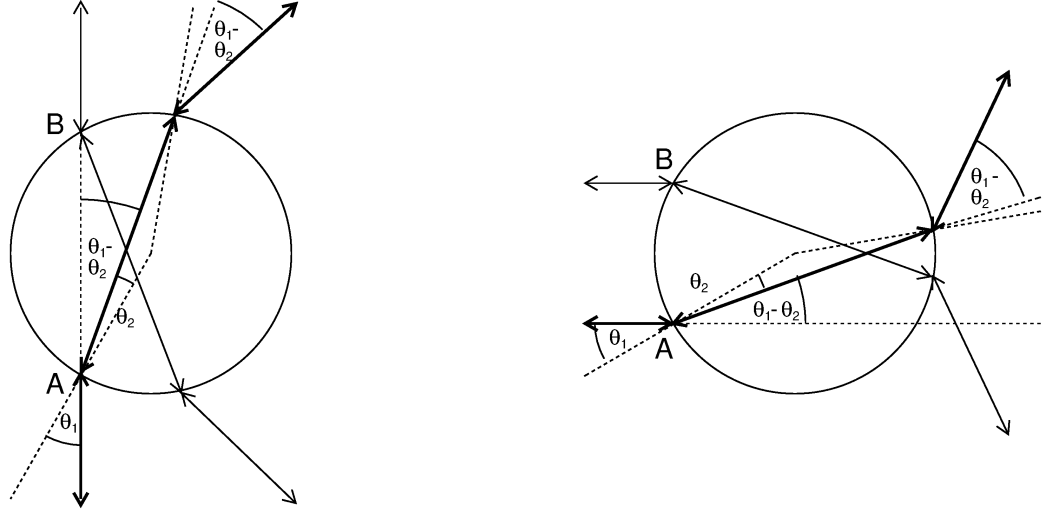


**Figure 2.** Wave motions around a dielectric sphere with refractive index  $n_2$ , embedded in a medium with refractive index  $n_1$ . Magnetic field and wave energy density gradient are in the vertical direction. The left panel shows the effect of parallel propagating waves. The bold arrows show a wave entering (or exiting) at point A, and being refracted downwards at both entrance and exit. A less energetic wave entering or exiting at point B is refracted upwards, but by a lesser amount, so that the net refraction of the wave is still downwards, resulting in an upwards force on the sphere, in the direction of  $-\partial U/\partial z$ , analogous to the FIP Effect. The right panel illustrates the case of a perpendicularly propagating fast mode wave. The wave entering at A is refracted upwards more than the wave entering at B, resulting in a downwards force on the sphere, in the direction of  $\partial U/\partial z$ . This is the origin of the Inverse FIP Effect.

For Alfvén waves, relating  $\partial U/\partial z$  to  $\delta E$  is relatively straightforward. Since Alfvén waves carry their energy along the magnetic field, and do not refract in increasing Alfvén speed like fast modes, we take the Poynting vector  $S = Uv_A$  for upward and downward going waves separately and assume  $S/B$  to be constant. Then

$$\frac{\partial}{\partial z} \left( \frac{S}{B} \right) = \frac{\partial U}{\partial z} \frac{v_A}{B} + U \frac{\partial}{\partial z} \left( \frac{v_A}{B} \right) = 0 \quad (8)$$

so that

$$\begin{aligned} \frac{\partial U}{\partial z} &= -\frac{UB}{v_A} \frac{\partial}{\partial z} \left( \frac{v_A}{B} \right) = -\frac{SB}{v_A^2} \frac{\partial}{\partial z} \left( \frac{\delta E^2}{B^2} \right) \frac{Bc^2}{8\pi S} \\ &= -\frac{\rho c^2}{2} \frac{\partial}{\partial z} \left( \frac{\delta E^2}{B^2} \right). \end{aligned} \quad (9)$$

In the limit  $n_2 \gg n_1$ , with  $\rho$  interpreted as the density inside the sphere, the acceleration is given by

$$a = \frac{3\pi c^2}{16} \frac{\partial}{\partial z} \left( \frac{\delta E^2}{B^2} \right), \quad (10)$$

different from the “exact” result in Equation 3 by a factor  $3\pi/8$ .

In the case of fast mode waves, expressing  $\partial U/\partial z$  in terms of  $\delta E^2$  is more involved. We take

$$\frac{\partial I_+}{\partial z} = -\frac{I_+}{v_A} \frac{\partial v_A}{\partial z} - I_+ \frac{\partial f_R}{\partial z} \quad (11)$$

$$\frac{\partial I_-}{\partial z} = -\frac{I_-}{v_A} \frac{\partial v_A}{\partial z} + I_+ \frac{\partial f_R}{\partial z} \quad (12)$$

where  $I_{\pm}$  are the intensities of upward and downward going waves and  $f_R = \sqrt{1 - 2c_s(z_{\beta=1})^2 / (v_A(z)^2 + c_s(z)^2)}$  represents the cumulative fraction of initially upward going waves refracted back downwards at altitudes  $z$  above the layer where  $\beta = 1$ ,  $z_{\beta=1}$  (Wood et al. 2012; Laming 2015a). Then forming  $\partial(I_+ - I_-)/\partial z$  and  $\partial(I_+ + I_-)/\partial z$  we find for the cross helicity,  $H$ , Poynting flux,  $S$ , and wave energy density  $U$ ,

$$\frac{\partial H}{\partial z} = \frac{\partial}{\partial z} \left( \frac{I_+ - I_-}{I_+ + I_-} \right) = -\frac{2I_+}{U} \frac{\partial f_R}{\partial z} \quad (13)$$

$$\frac{\partial S}{\partial z} = \frac{\partial}{\partial z} (I_+ - I_-) v_A = -2I_+ v_A \frac{\partial f_R}{\partial z} \quad (14)$$

$$\frac{\partial U}{\partial z} = \frac{\partial}{\partial z} (I_+ + I_-) = -\frac{U}{v_A} \frac{\partial v_A}{\partial z}. \quad (15)$$

With  $v_A = (c^2 \delta E^2 / 8\pi) H/S$  and assuming  $v_A \gg c_s$

$$\frac{\partial \ln H}{\partial z} = \frac{\partial \ln S}{\partial z} = \frac{\partial \ln (c_s^2/v_A^2)}{\partial z}, \quad (16)$$

after putting  $I_+ = I_0(1 - f_R)$  and  $I_- = I_+ f_R$ . We find

$$\frac{\partial U}{\partial z} = -\frac{c^2}{v_A^2} \frac{\partial}{\partial z} \left( \frac{\delta E^2}{8\pi} \right) - \frac{c^2 \delta E^2}{c_s^2 8\pi} \frac{\partial}{\partial z} \left( \frac{c_s^2}{v_A^2} \right) + \frac{c^2 \delta E^2}{v_A^2 8\pi} \frac{\partial \ln S}{\partial z} \quad (17)$$



where  $\gamma P$  in  $c_s^2 = \gamma P/\rho$  has been assumed constant in the term including  $\partial \ln H/\partial z$ . Pursuing these approximations, this term should cancel with the term in  $\partial \ln S/\partial z$  to leave only the first term. Neglecting the change in  $S$ , as we did for Alfvén waves, leaves only the first two terms contributing to the ponderomotive force which give Equation 9. Then from Equation 6 in the limit  $n_2 \gg n_1$  we find Equation 10 once more. Although the approximations in this approach are somewhat loose, we emphasize that this is the correct expression for the ponderomotive force due to fast modes, to within a factor  $3\pi/8$ , as evaluated with fuller mathematical rigor from Equation 3, which is the expression used in the modeling below.

Depending on the sign of  $\partial (\delta E^2/B^2)/\partial z$  Equations 3 or 10 admit FIP or Inverse FIP effect. Since  $B$  is usually decreasing with height, FIP effect (positive gradient) is more common, but if  $\delta E^2/B^2$  decreases with height, Inverse FIP fractionation can result. Such a solution requires strong reflection of initially upward propagating waves back downwards, and is generally only realistic for fast mode waves undergoing a total internal reflection. The best way to understand the physical basis for this trapping is to consider the now perpendicularly propagating fast mode waves, as in the right hand panel of Figure 1. The wave entering or exiting at point A refracts more energy upwards than the wave entering or exiting at point B, and hence the sphere is pushed downwards. So in a negative wave energy density gradient as before, the sphere is pushed *up* the gradient by the refraction of initially perpendicularly propagating waves, rather than down the gradient by initially parallel propagating waves. Calculating the refraction as before yields the negative of equation 6 for  $\Delta \dot{p}_\parallel$ . With zero Poynting vector, we write  $U = \rho c^2 \delta E^2/2B^2$  and remember that  $\rho$  refers to the density of the sphere (and not the surroundings), so that  $\partial U/\partial z = \rho c^2/2 \times \partial (\delta E^2/B^2)/\partial z$  which recovers Equation 10. These perpendicularly propagating fast modes most likely derive from the total internal reflection of an initially upward propagating wave field.

#### 4. FIP AND INVERSE-FIP MODELING FOR SOLAR FLARES

##### 4.1. Preamble

We return to the observations of solar flares (Dennis et al. 2015; Katsuda et al. 2020) and attempt to understand the abundance patterns seen in terms of the FIP and Inverse FIP effects on solar loops. We model shear Alfvén waves on a 100,000 km loop with 300 G magnetic field. The main difference in the models is the degree to which the magnetic field lines expand, and the magnetic field strength decreases, between the photo-

**Table 1.** Loop Models

$B_{cor}/B_{phot}$	ang. freq. (rad s <sup>-1</sup> )	$h_{\beta=1}$ (km)
0.3	1.0845	300
0.5	1.073	350
0.7	1.064	350

sphere and the corona. The equipartition layer, where gas and magnetic pressures are equal, lies in the middle of this magnetic field expansion. The models cited later on are given in Table 1. For constant coronal magnetic field, higher photospheric field results from greater expansion, and the loop resonant frequency is slightly higher due to the reduced travel time at the Alfvén speed from one footpoint to the other, although the equipartition layer lies a little lower. For all models, the Alfvén wave amplitude corresponds to a velocity perturbation of about 130 km s<sup>-1</sup> in the corona at a density of about  $4 \times 10^8$  cm<sup>-3</sup>. Higher coronal density,  $n_e$ , would lead to a lower coronal velocity perturbation, proportional to  $1/\sqrt{n_e}$  for a standing wave. A uniform upgoing slow mode wave energy flux of  $10^8$  ergs cm<sup>-2</sup> s<sup>-1</sup> deriving from photospheric convective motions is injected at the  $\beta = 1$  layer. The amplitude increases as the density decreases, according to the WKB approximation, until the slow mode wave amplitude reaches the local sound speed. At this point further WKB amplitude growth ceases, on the assumption that a shock will form and radiate away the excess kinetic energy.

##### 4.2. Fractionation Mechanism

Our discussion above suggests that the “usual” FIP effect should result from the ponderomotive force developed by parallel propagating Alfvén or fast mode waves. These are treated by integrating the Alfvén wave transport equations as in previous papers (Laming 2009, 2012, 2015a, 2017; Laming et al. 2019). The refraction of perpendicularly propagating fast mode waves gives the Inverse FIP effect. These are treated following Wood et al. (2012); Laming (2015a) as approximately isotropic in the upward moving hemisphere. At chromospheric height  $z$  the reflected fraction is approximately

$$f_R(z) \simeq \sqrt{1 - \frac{2c_S^2(z_{\beta=1})}{v_A^2(z) + c_S^2(z)}} \quad (18)$$

where  $z_{\beta=1}$  is the chromospheric height where mode conversion occurs. This is slightly different to the previous versions cited above in including the factor of 2 multiplying  $c_S^2(z_{\beta=1})$  in the numerator inside the square root. This gives  $f_R(z_{\beta=1}) = 0$  instead of  $1/\sqrt{2}$ , which reflect a presumed origin of fast mode waves as coming from

waves excited by sub-photospheric reconnection, rather than by convective motions. Convective motions would be ubiquitous, and upgoing and downgoing waves should be present in any chromospheric region. Waves from reconnection are spatially localized, and do not in general return to the  $\beta = 1$  layer at the same place where they left it.

We take the ponderomotive acceleration due to fast mode waves to be of the same form as that due to Alfvén waves,

$$a = \frac{c^2}{4} \frac{\partial}{\partial z} \left( \frac{\delta E^2}{B^2} \right) = \frac{\delta v^2}{2} (1 - f_R) \frac{1}{\delta v} \frac{\partial \delta v}{\partial z} - \frac{\delta v^2}{4} \frac{\partial f_R}{\partial z} \quad (19)$$

with variations in the acceleration arising due to the specific wave fields and propagation of the different modes. The two terms represent an upwards contribution arising as the fast mode waves increase in amplitude as they propagate through progressively lower density plasma, and the downwards contribution arising from fast mode wave reflection. Evaluating

$$\begin{aligned} \frac{\partial f_R}{\partial z} &= \frac{c_S^2 (z_{\beta=1}) v_A}{(v_A^2 + c_S^2)^2 f_R} \frac{\partial v_A}{\partial z} \\ &= \frac{c_S^2 (z_{\beta=1}) v_A^2}{(v_A^2 + c_S^2)^2 f_R} \left( \frac{1}{H_B} - \frac{1}{2H_D} \right) \end{aligned} \quad (20)$$

and assuming from the WKB approximation

$$\frac{1}{\delta v} \frac{\partial \delta v}{\partial z} = \frac{-1}{2H_B} - \frac{1}{4H_D}, \quad (21)$$

where  $H_D$  and  $H_B$  are the signed density and magnetic field scale heights, we find from Equation 19

$$\begin{aligned} a &= \frac{\delta v^2}{f_R} \left\{ (f_R - 1) \left( -\frac{1}{8H_D} - \frac{1}{4H_B} \right) \right. \\ &\quad \left. + \frac{c_S^2 (z_{\beta=1})}{(v_A^2 + c_S^2)^2} \left( -\frac{c_S^2}{8H_D} - \frac{c_S^2}{4H_B} - \frac{v_A^2}{2H_B} \right) \right\}. \end{aligned} \quad (22)$$

With both  $H_D$  and  $H_B$  negative and  $f_R < 1$ , the first term in curly brackets is negative, giving Inverse FIP effect. The second term is positive, giving positive FIP effect. In conditions where  $v_A \gg c_S$ , an overall downwards pointed ponderomotive acceleration requires  $|H_D| < |H_B|/2$  in this simple model.

The reflection of fast mode waves from other perturbations, e.g., density fluctuations caused by other waves or shocks (not included in this model) would increase the Inverse FIP effect developed. Even so, Equation 22 suggests that Inverse FIP effect is more likely to found in conditions with minimal magnetic field expansion through the chromosphere. This might correspond

with the conclusions of Baker et al. (2019, 2020) that sub-photospheric reconnection is required to generate the necessary waves to cause Inverse FIP, thus weakening the magnetic field low down in the atmosphere relative to that higher up. It might also fit with observations in M dwarfs. While the magnetic fields measured in these stars are similar to those in the Sun, the filling factor is higher (e.g., Donati & Landstreet 2009; Reinert et al. 2009), allowing less volume for expansion with increasing altitude.

#### 4.3. Charge Exchange

In modeling Inverse FIP fractionation, the ionization balance in the low chromosphere, where the ponderomotive force due to the fast mode waves develops, becomes crucial. This is dominated for many elements by charge exchange ionization by protons. We take most rates as the minimum of either the Langevin estimate (see Laming 2012) or the rate given by Kingdon & Ferland (1996). The Langevin rate is taken to be a theoretical maximum, so a rate larger than this must be in error, but the rate may be smaller given sufficient scarcity of final states for the captured electron. The Langevin estimate is also taken where rates are missing from the Kingdon & Ferland (1996) tabulation. Additionally, we take the charge exchange ionization of S from Zhao et al. (2005). Prior work (e.g. Laming et al. 2019, and its antecedents) had used the rate of Butler & Dalgarno (1980) and Le Teuff et al. (2000) in preference to the result tabulated by Kingdon & Ferland (1996), the discrepancy being about five orders of magnitude. At chromospheric temperatures, the rate of Zhao et al. (2005) is about three orders of magnitude larger than Kingdon & Ferland (1996), and two orders of magnitude lower than in our previous calculations. The ionization fraction of S is correspondingly lower than in for example Laming et al. (2019), but still sufficiently high that S is subject to the Inverse FIP effect. We also replace the charge exchange ionization rate for Na with the Langevin estimate, while the corresponding rate for Fe is reduced from the value given by Kingdon & Ferland (1996). The polarizabilities coming into the charge exchange rates, and also into the elastic scattering rates involving neutrals are taken from the tabulation of static polarizabilities of Schwerdtfeger & Nagle (2019).

#### 4.4. Results

Katsuda et al. (2020) collect 10 spectra from 4 X-class flares observed in 2005, and derive abundances from each spectrum using fits with two plasma components at different temperatures, and for comparison also employing a full differential emission measure (DEM) treat-

**Table 2.** Data and Models for [Katsuda et al. \(2020\)](#)

ratio	obs. abundance	$B_{cor}/B_{photo} = 0.3$				0.5				0.7			
		$v_{fm} = 0$	9	12	15	0	8	10	12	0	6	7	8
Si/H	0.76 [0.38 - 1.09]	2.71	2.13	1.77	1.39	2.55	1.22	0.80	0.48	2.79	1.26	0.95	0.68
S/H	0.39 [0.21 - 0.49]	1.33	1.11	0.96	0.81	1.26	0.67	0.58	0.31	1.35	0.68	0.54	0.40
Ar/H	0.86 [0.55 - 1.29]	1.08	1.08	1.08	1.08	1.03	1.03	1.03	1.03	1.11	1.11	1.11	1.11
Ca/H	1.89 [1.61- 2.29]	5.07	3.98	3.30	2.59	4.79	2.07	1.29	0.73	5.32	2.03	1.55	1.06
Fe/H		4.62	3.64	3.02	2.39	4.37	1.74	1.04	0.55	4.84	1.77	1.23	0.81

NOTE—Fast mode wave amplitudes at  $\beta = 1$  are in  $\text{km s}^{-1}$ . Coronal magnetic field  $B_{cor} = 300$  G. Abundance ratios are averages of 10 spectra from 4 flares, relative to photospheric abundances of ([Lodders 2003](#)). Ranges are minimum and maximum values from DEM analysis.

ment. Coronal abundances are compared with photospheric values from [Lodders \(2003\)](#). We take the average of the abundances deduced by the DEM method, and compare them with various models in Table 2. The Si abundance is taken to be the average of the abundances derived from Si XIII He $\alpha$  and Si XIV Lyman  $\alpha$ , while the S, Ar, and Ca abundance come from the He $\alpha$  transitions of the He-like ion of each element. The models in Table 1 are given for ratios of the coronal to photospheric magnetic field  $B_{cor}/B_{photo} = 0.3, 0.5$ , and  $0.7$ . For each value of  $B_{cor}/B_{photo}$ , abundances relative to H are tabulated for different values of the upgoing fast mode wave amplitude entering the  $\beta < 0$  region of the chromosphere at the equipartition layer. For zero fast mode wave amplitude, a standard FIP effect results due to the Alfvén waves in the model. As the fast mode wave amplitude is increased, the degree of FIP fractionation reduces, eventually becoming Inverse FIP at the highest fast mode wave amplitudes considered, for  $B_{cor}/B_{photo} = 0.5$  and  $0.7$ . The best match is probably achieved for  $B_{cor}/B_{photo} = 0.7$  with  $7 \text{ km s}^{-1}$  fast mode wave amplitude. S exhibits the strongest Inverse FIP effect, both in observations and in models. Si also shows Inverse FIP but to a lesser degree than S, Ar is essentially unchanged, while Ca retains positive FIP effect. For reference, and for comparison with the results of [Dennis et al. \(2015\)](#) to be discussed below, we also give the fractionations for Fe/H.

To illustrate more clearly the processes in our models, we show in Figure 3 the various features of the chromospheric model and wave fields that give rise to these fractionations. Top left (panel a) shows the background chromospheric model density and temperature profiles from [Avrett & Loeser \(2008\)](#). Top middle (panel b) and top right (panel c) show the ionization fractions for various low FIP and high FIP elements respectively. The change in the S charge exchange ionization rate has reduced the S ionization fraction from above 99% to about

94% in the upper regions of the chromosphere, falling to about 85-90% near the equipartition layer. There are of course several other processes that contribute to the S ionization balance, so that a two order of magnitude change in the charge exchange ionization rate results in only a  $\sim 10\%$  change in the ionization fraction.

Bottom left (panel d) shows the upward and downward Alfvén wave energy fluxes (in black), and the Alfvén wave energy density in red. Even though the Alfvén waves are chosen to be resonant with the loop, and have the largest amplitude in the coronal section of the model (not shown), the wave energy density is highest in the chromosphere and is monotonically declining with height. According to our discussion above in section 3, these are conditions where parallel propagating waves should give positive FIP effect. The strongest negative wave energy gradient is found in a short region at about 2150 km altitude, corresponding to the steep density and temperature gradients in the background chromospheric model in panel a. Bottom middle (panel e) shows the sum of the ponderomotive accelerations (in black), due to parallel propagating Alfvén waves giving a positive acceleration, and perpendicularly propagating fast mode waves resulting from the total internal reflection, giving negative acceleration, leading to Inverse FIP. The slow mode wave amplitude resulting from parametric excitation by the Alfvén wave driver is shown by the red dotted line. This appears squared in the denominator of the integrand in equation 1. Finally at bottom right (panel f) we show the resulting fractionations. All the low FIP elements and S are depleted just above the equipartition layer at 350 km by about the same amount by the negative ponderomotive acceleration associated with the fast mode wave total internal reflection. The other high FIP elements are not affected, being almost completely neutral at this altitude. At the top of the chromosphere, positive FIP effect acts on different ions in different amounts, depending sensitively on their ion-



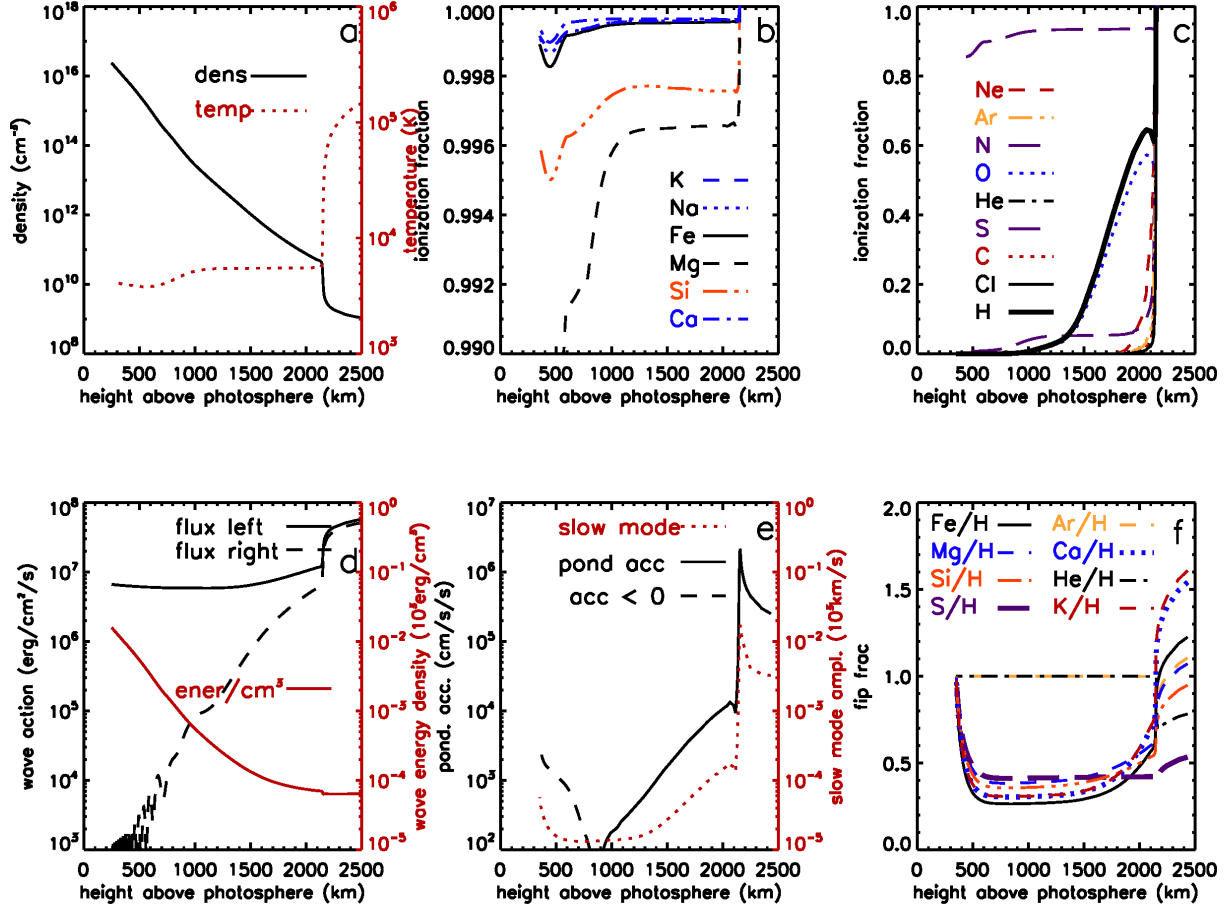


**Figure 3.** Chromospheric model and wave fields for FIP - Inverse FIP fractionation, shown for magnetic field expansion  $B_{cor}/B_{photo} = 0.7$ , fast mode wave speed at 350 km ( $\beta = 1$ )  $7 \text{ km s}^{-1}$ . Panel a gives density and temperature profiles, b gives ionization fractionation for low FIP elements, c ionization fractions for high FIP elements, d gives Alfvén wave energy fluxes for downgoing (left) and upgoing (right) waves in black, total wave energy in red, e gives total ponderomotive acceleration from both Alfvén (positive contribution) and fast mode waves (negative contribution) in black, parametrically driven slow mode wave amplitude in red, panel f gives element fractionations.

ization fractions, leading to overall positive FIP effect for Ca, and Inverse FIP for Si and S.

These effects can be understood with reference to Equation 1. In neutral background gas, the collision frequencies of ions and neutrals with the background,  $\nu_{kn} \sim \nu_{ki}$ , and the integrand depends simply on the ionization fraction  $\xi_k$ . Thus, the low FIPs and S, which all have  $\xi_k > 0.8$  are fractionated approximately the same in such conditions, and end up taking on similar Inverse FIP effects in the low chromosphere. Towards the top of the chromosphere where H is becoming ionized,  $\nu_{kn} \ll \nu_{ki}$ . Unless  $\xi_k$  is very close to unity, to the order of  $10^{-3}$  (approximately the ratio  $\nu_{kn}/\nu_{ki}$ ), the fractionation is suppressed by the back diffusion of neutrals. In such conditions, FIP fractionation favors the most highly ionized elements. Correspondingly, Ca is

fractionated the most, followed by Fe and Si. S, ionized to about 95%, is not FIP fractionated at all in this region.

Dennis et al. (2015) measure abundances for Si, S, Ar, Ca and Fe from 526 flares observed by the Solar Assembly for X-rays (SAX), part of the X-ray Spectrometer (XRS: Schlemm et al. 2007) on the MESSENGER mission. Table 3 gives their results for the 2007 June 1 flare, for the average of 526 flares observed between 2007 and 2013, and results for coronal abundances of Si, S, Ar, and K from the RESIK X-ray crystal spectrometer flown on the *Coronas-F* satellite (Sylwester et al. 2014) and for Fe from *RHESSI* observations (Phillips & Dennis 2012). These coronal abundances are compared with photospheric values from Asplund et al. (2009). These are in general lower than the results of Ludders (2003),

**Table 3.** Data and Models for [Dennis et al. \(2015\)](#)

ratio	observations			models for $B_{cor}/B_{photo} = 0.7$		
	RESIK	SAX	SAX	160 km s <sup>-1</sup>	193 km s <sup>-1</sup>	225 km s <sup>-1</sup>
	RHESSI	2007 June 1	2007-13	7 km s <sup>-1</sup>	9 km s <sup>-1</sup>	10 km s <sup>-1</sup>
Si/H	2.34	1.09	1.64±0.66	1.46	1.15	1.02
S/H	1.10	0.78	1.23±0.45	0.58	0.35	0.23
Ar/H	1.10	1.48	2.48±0.90	1.13	1.17	1.00
K/H	6.76			3.59	3.77	4.74
Ca/H	3.89	3.59	3.89±0.76	3.39	3.48	4.30
Fe/H	2.57	1.70	1.66±0.34	2.56	2.28	2.50

NOTE—Fast mode wave amplitudes at  $\beta = 1$  are in km s<sup>-1</sup>. Abundance ratios are averages of 526 flares, relative to photospheric abundances of ([Asplund et al. 2009](#)).

(used by [Katsuda et al. 2020](#)), by amounts ranging from 5% for Ca/H to 30% for Ar/H, leading to higher fractionations reported by [Dennis et al. \(2015\)](#), relative to [Katsuda et al. \(2020\)](#), by amounts comparable to or less than the reported fractionation uncertainties. [Dennis et al. \(2015\)](#) speculate that the division between low FIP and high FIP elements may move in flares from the usual 10 eV (i.e. those elements that can be ionized by H I Lyman  $\alpha$ ) to a value more like 7 eV, but do not specify a mechanism. We argue instead that the peculiar abundance enhancement pattern is a combination of Inverse FIP effect low down in the chromosphere, a feature only present in solar flares, and the more usual FIP effect at the top of the chromosphere where the background gas is becoming ionized. Table 3 compares the abundance fractionations from [Dennis et al. \(2015\)](#) with models calculated for  $B_{cor}/B_{photo} = 0.7$ , with varying coronal Alfvén wave amplitude (160 - 225 km s<sup>-1</sup>) and fast mode wave amplitude at the equipartition layer (7 - 10 km s<sup>-1</sup>). [Dennis et al. \(2015\)](#) only see an Inverse FIP for S during the 2007 June 1 flare, but in all other cases S is the least enhanced. But combined with the insights gained from the analysis of [Katsuda et al. \(2020\)](#), the combination of FIP and Inverse FIP offers a plausible explanation of these observations. Similarly, [Warren \(2014\)](#) measured an Fe abundance enhancement of  $1.17 \pm 0.22$  from 640 spectra taken during 21 flares during the solar maximum of 2011-13, using the Solar Dynamics Observatory Extreme-ultraviolet Variability Experiment (SDO/EVE). With just one datum, [Warren \(2014\)](#) argued that during flares, chromospheric evaporation must originate deep in the chromosphere, below the region where FIP fractionation occurs. But the fractionation observed is also consistent with our modeling in Table 2 where the [Katsuda et al. \(2020\)](#) observations make it clear the Inverse FIP effect is at work.

## 5. DISCUSSION AND CONCLUSIONS

There are many possible processes that might reduce the degree of FIP fractionation from the usual factor of about 3 seen in active region and the solar wind to lower values seen in solar flares. Either a lower Alfvén wave amplitude, or a significant upward flow velocity ( $u_k$  in Equation 1; [Laming 2017](#)) and its associated effects on fractionation and slow mode wave production, could reasonably be expected in solar flare plasmas. However Inverse FIP fractionation as seen by [Doschek et al. \(2015\)](#); [Doschek & Warren \(2016\)](#) in localized regions and by [Katsuda et al. \(2020\)](#) in spatially unresolved solar flare plasma requires a quite different explanation. One of the early attractive features of the ponderomotive force ([Laming 2004](#)) was that given suitable wave fields, it could point upward or downward, giving FIP or Inverse FIP fractionation respectively. Calculations with parallel propagating Alfvén waves have difficulty achieving the degree of wave reflection required to give a plausible Inverse FIP effect. Fine-tuning of wave frequencies far beyond what is realistic for the solar chromosphere is required, which then leads to the idea of the total internal reflection of fast mode waves as a means of generating downward pointing ponderomotive force.

The fast modes most likely originate as sound waves from the photosphere that mode-convert into fast modes at the equipartition layer. However the fast mode wave amplitudes quoted above at the equipartition layer are significantly larger than those expected to derive from waves associated with photospheric convection. In our models above, an acoustic wave energy flux of  $10^8$  ergs cm<sup>-2</sup> s<sup>-1</sup> gives an acoustic wave amplitude of order 1 km s<sup>-1</sup> at a density of  $2 \times 10^{16}$  cm<sup>-3</sup> at an altitude of 300 km, comparable to amplitudes observed ([Stangalini et al. 2012](#)), whereas fast mode wave amplitudes of several times this value are required in Tables 2 and 3. [Baker et al. \(2019\)](#) identified the small patches of Inverse FIP plasma observed in the corona during a flare with sub-photospheric reconnection between two inter-

acting sunspots. [Baker et al. \(2020\)](#) investigate further, and find regions of Inverse FIP effect plasma coinciding with strong light bridges within sunspot umbrae. [Kigure et al. \(2010\)](#) have investigated MHD wave generation by reconnection, and following this work, the geometry of reconnection at the light bridge suggests that mainly Alfvén waves, not sound waves, should have been produced. These would propagate upward along the magnetic field through the equipartition layer without mode conversion here to fast modes. Such mode conversion can happen elsewhere if the inclination of the magnetic field to the vertical direction rotates, such that the Alfvén wave polarization is rotated to become fast mode.

Flare plasma arrives in the corona through the process of chromospheric evaporation. As mentioned above, the term in  $u_k$  representing the flow velocity of element  $k$  reduces the fractionation when this begins to dominate the denominator in the integrand of Equation 1, which typically occurs in the range 1 - 10 km s<sup>-1</sup>. Such flow speeds (or higher) are more likely to be realized in the lower density gas in the upper layers of the chromosphere (assuming constant evaporative mass flux) and so we might expect the FIP fractionation to be more affected than the Inverse FIP fractionation, because this last process occurs in the lower chromosphere where flow speeds will be lower. In fact upward flow speeds are likely to be significantly higher than 1 - 10 km s<sup>-1</sup>, and

the most plausible scenario for FIP fractionation seems to be case modeled by [Dahlburg et al. \(2016\)](#). Explosive events in the flaring loop release heat and Alfvén waves. In conditions where the Alfvén speed is greater than the electron thermal speed, corresponding to minimum magnetic field strengths in the range 30 - 100 G, the Alfvén waves reach the chromosphere first and fractionate the plasma before the heat flux arrives to cause the evaporation. An episodic heating process should allow fractionation with large evaporative velocities, and suggest that active regions should show stronger FIP fractionation than quiet solar corona where the magnetic field is weaker.

The ponderomotive acceleration model of the FIP effect also appears to provide a satisfactory explanation of the Inverse FIP bias. Nothing more exotic than a source of fast mode waves at the equipartition layer, and the apparent shift of the boundary between low FIP and high FIP elements arises naturally. Our results indicate that Inverse FIP fractionation in flares could be common, having been generally masked by the competing FIP fractionation, possibly suggesting a role for sub-photospheric reconnection in the flare process.

#### ACKNOWLEDGMENTS

This work has been supported by the NASA Heliophysics Guest Investigator (80HQTR19T0029) and Supporting Research Programs (80HQTR20T0076), and by Basic Research Funds of the Office of Naval Research.

### APPENDIX

#### A. TURBULENT CASCADE RATE FROM QUASI-LINEAR THEORY

In anisotropic turbulence, the three wave interaction for  $P + Q \longleftrightarrow M$  with wavevectors  $\mathbf{k}_1$ ,  $\mathbf{k}_2$ , and  $\mathbf{k}$  is allowed if  $\omega_P \simeq \omega_M$  and  $\omega_Q \rightarrow 0$ . We sketch the calculation of this interaction rate from quasi-linear plasma theory, following [Melrose \(1986\)](#) and [Luo & Melrose \(2006\)](#). The rate equation for the evolution of the number of plasma quanta in mode  $M$ ,  $N_M$ , is

$$\frac{dN_M(\mathbf{k})}{dt} = 4(4\pi)^3 \hbar \int \frac{R_M(\mathbf{k}) R_P(\mathbf{k}_1) R_Q(\mathbf{k}_2)}{\omega_M(\mathbf{k}) \omega_P(\mathbf{k}_1) \omega_Q(\mathbf{k}_2)} |\mathbf{e}_{Mi} \mathbf{e}_{Pj} \mathbf{e}_{Ql} \alpha_{ijl}|^2 N_P(\mathbf{k}_1) N_Q(\mathbf{k}_2) (2\pi)^4 \quad (\text{A1})$$

$$\times (2\pi)^4 \delta^4(k - k_1 - k_2) \delta(|\mathbf{k}| - |\mathbf{k}_1|) \frac{d^3 \mathbf{k}_1}{(2\pi)^3} \frac{d^3 \mathbf{k}_2}{(2\pi)^3} \quad (\text{A2})$$

where  $R_M = v_A^2/2c^2$  etc is the ratio of electric to total energy in the wave, and  $\mathbf{e}_{Mi}$  etc are the wave polarization vectors. The second delta function  $\delta(|\mathbf{k}| - |\mathbf{k}_1|)$  incorporates the requirement  $\omega_Q \rightarrow 0$ . From [Melrose \(1986\)](#) Equation 10.9 where  $\omega_Q \ll \omega_M, \omega_P$ , we put for the quadratic response tensor

$$\alpha_{ijl} = -\frac{e^3 n}{2m^2 \omega_Q} \{k_r \tau_{rl}(\omega_Q) \tau_{ij}(\omega_P) - k_{1r} \tau_{rl}(\omega_Q) \tau_{ij}(\omega_M)\}, \quad (\text{A3})$$

where in the limit  $\omega \ll \Omega = eB/mc$ , the ion cyclotron frequency,

$$\tau_{ij}(\omega) = \begin{bmatrix} -\frac{\omega^2}{\Omega^2} & -i\epsilon\frac{\omega}{\Omega} & 0 \\ i\epsilon\frac{\omega}{\Omega} & -\frac{\omega^2}{\Omega^2} & 0 \\ 0 & 0 & 1 \end{bmatrix}. \quad (\text{A4})$$

We choose  $\mathbf{k} = (k_\perp, 0, k_\parallel)$ ,  $\mathbf{k}_1 = (k_{1\perp} \cos \phi_1, k_{1\perp} \sin \phi_1, k_{1\parallel})$ , and  $\mathbf{k}_2 = (k_{2\perp} \cos \phi_2, k_{2\perp} \sin \phi_2, k_{2\parallel})$  so with  $\mathbf{k} = \mathbf{k}_1 + \mathbf{k}_2$

$$\alpha_{ijl} \simeq -\frac{e^3 n}{2m^2 \omega_Q} \{k_{2\perp} \cos \phi_2 \tau_{xl}(\omega_Q) \tau_{ij}(\omega_P) + k_{2\perp} \sin \phi_2 \tau_{yl}(\omega_Q) \tau_{ij}(\omega_M)\}. \quad (\text{A5})$$

With  $\mathbf{e}_M = (1, 0, 0)$ ,  $\mathbf{e}_P = (\cos \phi_1, \sin \phi_1, 0)$ , and  $\mathbf{e}_Q = (\cos \phi_2, \sin \phi_2, 0)$

$$\alpha_{ijl} \mathbf{e}_{Mi} \mathbf{e}_{Pj} \mathbf{e}_{Ql} = -\frac{e^3 n k_{2\perp} \omega_Q}{2m^2 \Omega^2} \left\{ \frac{\omega^2}{\Omega^2} \cos \phi_1 + i\epsilon \frac{\omega}{\Omega} \sin \phi_1 \right\}, \quad (\text{A6})$$

so with ion plasma frequency  $\omega_p^2 = 4\pi e^2 n/m$ ,  $v_A^6 \omega_p^6 = c^6 \Omega^6$ , and  $\omega \ll \Omega$

$$\frac{dN_M(\mathbf{k})}{dt} = \frac{1}{8} \int k_{2\perp}^2 \frac{\hbar \omega_Q N_Q(\mathbf{k}_2)}{nm} N_P(\mathbf{k}_1) \delta^3(\mathbf{k} - \mathbf{k}_1 - \mathbf{k}_2) \delta(\omega_M - \omega_P - \omega_Q) \delta(|\mathbf{k}| - |\mathbf{k}_1|) \sin^2 \phi_1 \frac{d^3 \mathbf{k}_1}{2\pi} \frac{d^3 \mathbf{k}_2}{2\pi}. \quad (\text{A7})$$

Putting  $\rho \delta v_\perp^2 / 2 = \int \hbar \omega_Q N_Q d^3 \mathbf{k}_2 / (2\pi)^3 \simeq \hbar \omega_Q N_Q 2\pi k_{2\perp}^2 |k_{2\parallel}| / (2\pi)^3$  we find

$$\frac{dN_M(\mathbf{k})}{dt} = \frac{1}{16} \int \frac{\delta v_\perp^2}{|k_{2\parallel}|} N_P(\mathbf{k}_1) \delta^3(\mathbf{k} - \mathbf{k}_1 - \mathbf{k}_2) \delta(\omega_M - \omega_P - \omega_Q) \delta(|\mathbf{k}| - |\mathbf{k}_1|) \sin^2 \phi_1 d^3 \mathbf{k}_1 d^3 \mathbf{k}_2 \quad (\text{A8})$$

$$= \frac{1}{32\pi} \int \frac{\delta v_\perp^2}{|k_\parallel - k_{1\parallel}| v_A} N_P(\mathbf{k}_1) \delta(|\mathbf{k}| - |\mathbf{k}_1|) \sin^2 \phi_1 d^3 \mathbf{k}_1 \quad (\text{A9})$$

$$= \frac{1}{64} \frac{k_{1\perp}^2 \delta v_\perp^2}{(1 - \cos \psi) k_\parallel v_A} N_P(\mathbf{k}_1) \quad (\text{A10})$$

in the special case that  $k_\perp = 0$ . This recovers the heuristic expression for  $k \sim k_1$  and  $1 - \cos \psi = 1/64$  or  $\psi \simeq 1/4\sqrt{2}$ , where  $\psi$  is the angle between  $\mathbf{k}$  and  $\mathbf{k}_1$ . With  $N_M \propto \delta v_\perp^2 \propto k_\perp^{-\alpha}$ , Equation A10 gives  $\alpha = 2$ , and the cascade rate  $\gamma \propto k_\perp^2 \delta v_\perp^2$  is constant with  $k_\perp$ .

## REFERENCES

- Ashkin, A. 1970, *Phys. Rev. Lett.*, 24, 156
- Ashkin, A., Dziedzic, J. M., Bjorkholm, J. E., & Chu, S. 1986, *Optics Letters*, 11, 288
- Asplund, M., Grevesse, N., Sauval, A. J., & Scott, P. 2009, *ARA&A*, 47, 481
- Athay, R. G. 1981, *ApJ*, 249, 340
- Avrett, E. H., & Loeser, R. 2008, *ApJS*, 175, 229
- Batchelor, G. K. 1986, *The Theory of Homogenous Turbulence* (Cambridge: Cambridge University Press)
- Baker, D., van Driel-Gesztelyi, L., Brooks, D. H., Démoulin, P., Valori, G., Long, D. M., Laming, J. M., To, A. S. H., & James, A. W. 2020, *ApJ*, 894, 35
- Baker, D., van Driel-Gesztelyi, L., Brooks, D. H., Valori, G., James, A. W., Laming, J. M., Long, D. M., Démoulin, P., Green, L. M., Matthews, S. A., Oláh, K., & Kovári, Z. 2019, *ApJ*, 875, 35
- Beresnyak, A. 2019, *Living Rev. Comp. Astrophys.*, 5, 2
- Butler, S. E., & Dalgarno, A. 1980, *A&A*, 85, 144
- Dahlburg, R. B., Laming, J. M., Taylor, B. D., & Obenshain, K. 2016, *ApJ*, 831, 160
- Dennis, B. R., Phillips, K. J. H., Schwartz, R. A., Tolbert, A. K., Starr, R. D., & Nittler, L. R. 2015, *ApJ*, 803, 67
- Donati, J.-F., & Landstreet, J. D. 2009, *Ann. Rev. Astron. Astrophys.*, 47, 333
- Doschek, G. A., Warren, H. P., & Feldman, U. 2015, *ApJL*, 808, L7
- Doschek, G. A., & Warren, H. P. 2016, *ApJ*, 825, 36
- Doschek, G. A., & Warren, H. P. 2017, *ApJ*, 844, 52
- Drake, J. J., Laming, J. M., & Widing, K. G. 1997, *ApJ*, 478, 403
- Feldman, U., Widing K. G., & Lund P. A. 1990, *ApJL*, 364, L21

- Katsuda, S., Ohno, M., Mori, K., et al. 2020, *ApJ*, 891, 126
- Kigure, H., Takahashi, K., Shibata, K., Yokoyama, T., & Nozawa, S. 2010, *PASJ*, 62, 993
- Kingdon, J. B., & Ferland, G. J. 1996, *ApJS*, 106, 205
- Koyama, K., Tsunemi, H., Dotani, T., et al. 2007, *PASJ*, 59, 23
- Laming, J. M., Vourlidas, A., Korendyke, C., et al. 2019, *ApJ*, 879, 124
- Laming, J. M. 2017, *ApJ*, 844, 153
- Laming, J. M. 2015, *Living Reviews in Solar Physics*, 12, 2
- Laming, J. M. 2015, *ApJ*, 805, 102
- Laming, J. M. 2012, *ApJ*, 744, 115
- Laming, J. M. 2009, *ApJ*, 695, 954
- Laming, J. M. 2004, *ApJ*, 614, 1063
- Laming, J. M., & Drake, J. J. 1999, *ApJ*, 516, 324
- Laming, J. M., Drake, J. J., & Widing, K. G. 1996, *ApJ*, 462, 948
- Laming, J. M., Drake, J. J., & Widing, K. G. 1995, *ApJ*, 443, 416
- Landau, L. D., & Lifshitz, E. M. 1987, *Fluid Mechanics* (Oxford: Pergamon)
- Lee, N. C., & Parks, G. K. 1983, *Phys. Fluids*, 26, 724
- Le Teuff, Y. H., Millar, T. J., & Markwick, A. J. 2000, *A&AS*, 146, 157
- Lodders, K. 2003, *ApJ*, 591, 1220
- Lundin, R., & Guglielmi, A. 2006, *SSRv*, 127, 1
- Luo, Q., & Melrose, D. 2006, *MNRAS*, 368, 1151
- Melrose, D. B. 1986, *Instabilities in Space and Laboratory Plasmas* (Cambridge: Cambridge University Press)
- Mitsuda, K., Bautz, M., Inoue, H., et al. 2007, *PASJ*, 59, 1
- Ng, C. S., & Bhattacharjee, A. 1997, *Phys. Plasmas*, 4, 606
- Peierls, R. 1991, *More Surprises in Theoretical Physics* (Princeton: Princeton University Press)
- Phillips, K. J. H., & Dennis, B. R. 2012, *ApJ*, 748, 52
- Pottasch, S. R. 1963, *ApJ*, 137, 945
- Reardon, K. P., Lepreit, F., Carbone, V., & Vecchio, A. 2008, *ApJL*, 683, L207
- Reiners, A., Basri, G., & Browning, M. 2009, *ApJ*, 692, 538
- Ridpath, I. 1985, *A Comet Called Halley* (Cambridge: Cambridge University Press)
- Schlemm, C. E., Starr, R. D., Ho, G. C., et al. 2007, *SSRv*, 131, 393
- Schwerdtfeger, P., & Nagle, J. K. 2019, *Molecular Phys.*, 117, 1200
- Stangalini, M., Giannattasio, F., Del Moro, D., & Berrilli, F. 2012, *A&A*, 539, L4
- Sylwester, B., Sylwester, J., Phillips, K. J. H., Kępa, A., & Mrozek, T. 2014, *ApJ*, 787, 122
- Warren, H.P. 2014, *ApJL*, 786, L2
- Washimi, H., & Karpman, V. I. 1976, *JETP*, 44, 528
- Wood, B. E., Laming, J. M., Warren, H. P., & Poppenhager, K. 2018, *ApJ*, 862, 66
- Wood, B. E., Laming, J. M., & Karovska, M. 2012, *ApJ*, 753, 76
- Zhao, L. B., Stancil, P. C., Gu, J.-P., Liebermann, H.-P., Funke, P., Buenker, R. J., & Kimura, M. 2005, *Phys. Rev. A*, 71, 062713